Supporting Information

Hood et al. 10.1073/pnas.1603788113

SI Text

In our results in the main text, we measure collective frequency shifts and decay rates for atoms trapped near a PCW. In our previous work in ref. 21, we trapped multiple atoms in an optical dipole force trap above the PCW. We operated with the atomic frequency outside the bandgap in a regime with large decay rate Γ_{1D} and small coherent coupling rate J_{1D}. By varying the density and observing the superradiant decay of the atoms $\Gamma_{tot}^{(\bar{N})} = \Gamma_{SR}(\bar{N}) + \Gamma_{1D} + \Gamma'$, we inferred the single-atom GM decay rate Γ_{1D} and the average number of atoms $\bar{N}$. Importantly, this measured single-atom decay rate Γ_{1D} agreed well with the FDTD simulations at the calculated trap location. This good agreement is in part because of the nanometer-scale accuracy in which the alligator PCWs are fabricated, which is required for both the band edge alignment and the device quality.

In our paper, the band edge of the PCW is tuned around the resonance frequency of the atoms, and we observe the dominance of the GM-coherent coupling rates J_{1D} over the dissipative coupling rates Γ_{1D}, which is associated with atomic radiative processes for operation within the bandgap. To extract quantitative values for these parameters from our measurements of transmission spectra for atoms trapped along a PCW, we have developed theoretical techniques based on Green's functions for the PCW, which are new to atomic physics. As in ref. 21, the average number of atoms $\bar{N}$ is measured by way of transient decay. Our principal finding relates to the turning off of the GM decay rate Γ_{1D}, which in the bandgap, is predicted to be exponentially suppressed, while nonetheless, retaining appreciable coherent processes described by J_{1D}.

For the spectra in our paper, the transmission through the device decreases exponentially in the bandgap, and more time is required to measure the transmission spectra compared with our work in ref. 21. Unfortunately, Cs slowly coats the PCW during the measurement, both degrading the device quality and shifting the band edge out of the thermal tuning range. As a result, each device only has a limited lifetime for making transmission measurements. For our experiment, we first repeated superradiance measurements outside the bandgap at the first resonance ν_1 of the PCW to determine the average number of atoms $\bar{N}$ and the single-atom GM decay rate Γ_{1D} and show that the atoms behave as a collective emitter. Then, with an average number of $\bar{N} \simeq 3$, we measured transmission spectra as the atomic frequency is shifted into the bandgap. We simultaneously measured the TM spectra to verify that the atom number is constant over the course of the measurements of the TE spectra.

1. Alligator PCW Design and Fabrication. The schematic of the device is shown in Fig. S1*A*. Light is coupled into and out of the device by mode-matching the output of an optical fiber to that of a terminated rectangular-shaped waveguide on both sides of the device (33). The fibers are glued permanently in etched v grooves at optimized coupling positions. The design and fabrication of the alligator PCW are detailed in ref. 33. The PCW is fabricated on a 200-μm Si chip coated with a 200-nm-thick SiN film. The SiN device is suspended across a 2-mm-wide window after the Si substrate beneath it is removed, as shown in the image in Fig. S1*B*. The window allows optical access for the trapping and cooling of atoms around the device.

The dielectric TE mode band edge (ν_{BE}) is aligned to within 200 GHz of the Cs D_1 line ($\nu_{D1} = 335.12$ THz) by a low-power inductively coupled reactive ion CF_4 etch. The directional etch thins the SiN layer at a rate of 3 nm/min until a transmission measurement confirms alignment of the band edge. The final geometric dimensions of the device used in the text are given in Fig. S1*C*.

For the experiment, the chip is placed at the center of an ultrahigh vacuum chamber, and the optical fibers exit through Teflon fiber feedthroughs. We measure the transmission through a device using a superluminescent diode as the source and an optical spectrum analyzer as the detector. The measured transmission and reflection spectra are shown in Fig. S2*A*. The transmission spectra near the lower (dielectric) and upper (air) band edges are compared with an FDTD simulation in Fig. S2 *B* and *C*.

2. Alligator Dispersion Relation from Scattering Images. Here, we describe the analysis performed for the PCW dispersion relations in Fig. 2*E*. We send a single-frequency laser beam through the device and image the scattered light with a microscope. We integrate the image over the width of the PCW to produce a single plot of intensity vs. position. Then, we scan the laser frequency around the lower band edge to produce a 2D plot of scattered intensity as a function of position x along the device and frequency ν of the input light.

The weak scattered light comes from small fabrication imperfections or intrinsic material defects and serves as a probe of the local intensity. Because each scatterer emits light at a different rate, we have to normalize the scattered light by a reference intensity spectrum in which the intensity of the device is known. For this reference spectrum, we average over the intensities for frequencies far from the band edge, where the PCW behaves like a waveguide and the local intensity in the device is approximately constant. The normalized data are shown in Fig. S3, and a zoomed-in version is in Fig. 2*A*.

In the FDTD simulation described above, we calculate the intensity along the center of the device for frequencies around the band edge. Taking the maximum intensity in each unit cell and normalizing by the intensity in the waveguide regime, we produce Fig. 2*B*.

Next, we fit the intensity spectrum at a given frequency to a model to extract the wavevector for that frequency. Near the band edge, the field in an infinite PCW is well-approximated by $E(x) \propto \cos(x\pi/a)e^{i\delta k_x x}$, where $\delta k_x = \pi/a - k_x$ in the propagating band ($\Delta_{BE} < 0$) and $\delta k_x = i\kappa_x$ inside the bandgap ($\Delta_{BE} > 0$). The edges of a finite photonic crystal reflect with R_t because of a large group index mismatch between the waveguide section and the PCW. The resonances of the weak cavity result in the cavity-like intensity profiles seen at frequencies $\nu_{1,2,3,4,5}$ in Fig. S3. The intensity at a point x along a finite photonic crystal of length L is well-approximated by a model based on the intensity in a cavity with two mirrors of reflectivity R_t:

$$|E(x)|^2 = I_1 \left| e^{i\delta k_x x} - R_t e^{2i\delta k_x L} e^{-i\delta k_x x} \right|^2, \qquad \text{[S1]}$$

where I_1 is related to the overall intensity. This expression ignores the fast oscillations of the Bloch function, which go as $\cos^2(x\pi/a)$. Note that in the bandgap (when $\kappa_x L \gg 1$), the intensity model reduces to an exponential decay: $|E(x)|^2 \approx I_1\, e^{-2\kappa_x x}$. Interestingly, at the band edge ($\delta k_x \to 0$ and $R_t \to 1$), the intensity displays a quadratic dependence on the position: $|E(x)|^2 \propto (L - x)^2$.

For each frequency, we fit the intensity along the nominal cells with Eq. **S1** and extract δk_x. This procedure allows us to map out the dispersion relation $\delta k_x(\Delta_{BE})$, which we show in Fig. 2*E* for the measured and simulated data. From the simulated fits, we find that the effective length of the cavity is 162 cells, which is slightly longer than the 150 nominal cells and is expected due to the leakage of the cavity field into the tapering sections. We use this length for the fits of the measured data. Examples of the measured and simulated intensities are shown in Fig. S4. The fluctuation of the intensity, even after the normalization, is most likely caused by the spatial profile of Bloch mode. The normalization

trace is taken by averaging data for excitation frequencies farther away from the band edge where the Bloch mode contrast is reduced, whereas the data closer to the band edge have a large Bloch mode fringe visibility. However, the fluctuations do not affect the statistical fits at the level of accuracy required for the dispersion relation in this work.

The frequency for which $\delta k_x = 0$ is defined as the band edge frequency ν_{BE}. To extract this frequency and the curvature of the dispersion relation near the band edge, we fit the measured and simulated dispersion relations with a dispersion model (21),

$$\delta k_x(\nu) = \frac{2\pi}{a}\sqrt{\frac{(\nu_{\mathrm{BE2}}-\nu)(\nu_{\mathrm{BE}}-\nu)}{4\zeta^2-(\nu_{\mathrm{BE2}}-\nu_{\mathrm{BE}})^2}}, \qquad \textbf{[S2]}$$

where ν_{BE} (ν_{BE2}) is the lower (upper) band edge frequency, and ζ is a frequency related to the curvature of the band near the band edge. From the measured data fits, the distance between the first resonance and band edge is $\nu_{\mathrm{BE}} - \nu_1 = 133 \pm 9$ GHz and $\zeta = 227 \pm 3$ THz. The simulated data give $\nu_{\mathrm{BE}} - \nu_1 = 135.0$ GHz, and the curvature parameter is $\zeta = 226.0$ THz. These values are in good agreement with the dispersion relation from the eigenmode simulation of the infinite PCW in Fig. 1*C*, which gives $\zeta = 229.1$ THz.

3. SI Trap. In Fig. S5*A*, we show a schematic of the SI trap. The SI beam is nearly perpendicular to the axis of the device, has a 50-μm diameter, and has a polarization aligned to the axis of the device (Fig. S5*A*). The orange areas in Fig. S5*A* represent the approximate localization of the atoms along x,y. By time of flight measurements of atoms in the dipole trap, we estimate an atomic temperature of ∼30 μK. From the beam waist and atom temperature, we can infer that the atoms are localized to $2\Delta x_A = 12$ μm along the x axis.

Simulations of the SI trap potential are shown in Fig. S5 *B*–*D*. The simulations are performed for the infinite structure with COMSOL. The trap depth is calibrated with the 12-MHz AC Stark shift measured from the atomic spectra. Fig. S5*B* shows the trap potential in the y–z plane. Atoms that are significantly hotter than ∼100 μK are expected to crash into the device along the diagonal directions because of Casimir–Polder forces. Fig. S5*C* shows the trapping potential along the z axis. Atoms are trapped at $z = 240$ nm. Fig. S5*D* shows the trap along the x axis. Because of the photonic crystal, the trap modulates by ∼10 μK along the x axis, which is significantly smaller than the estimated trap temperature.

In addition to the results in Fig. S5, we have also carried out numerical modeling of the optical trap using Lumerical simulations (37) of the actual finite length PCW and tapers shown in Fig. S1. We have as well included Casimir–Polder potentials as in ref. 47. More details of the trap are discussed in ref. 21.

4. Transmission Model and Atomic Spectra Fits. Here, we give a more detailed description of the transmission model in the text, which follows the derivation given in ref. 39. A system of N atoms coupled to a radiation field can be described using formalism based on the classical Green's function (42, 43). In the Markovian limit, the field can be eliminated to obtain a master equation that describes the interactions between the atoms: $\dot{\hat{\rho}}_A = -i/\hbar[H, \hat{\rho}_A] + \mathcal{L}[\hat{\rho}_A]$. Here, the Hamiltonian H gives the coherent evolution of the system:

$$H = -\hbar\sum_{j=1}^{N}\tilde{\Delta}_A\hat{\sigma}_{ee}^{j} - \hbar\sum_{j,i=1}^{N}J_{1\mathrm{D}}^{ji}\hat{\sigma}_{eg}^{j}\hat{\sigma}_{ge}^{i} - \hbar\sum_{j=1}^{N}\left(\Omega_j\hat{\sigma}_{eg}^{j} + \Omega_j^{*}\hat{\sigma}_{ge}^{j}\right), \qquad \textbf{[S3]}$$

and the Lindblad operator $\mathcal{L}[\hat{\rho}_A]$ gives the dissipation of the system:

$$\mathcal{L}[\rho_A] = \sum_{j,i=1}^{N}\frac{\Gamma'\delta_{ji} + \Gamma_{1\mathrm{D}}^{ji}}{2} \times (2\hat{\sigma}_{ge}^{j}\hat{\rho}_A\hat{\sigma}_{eg}^{i} - \hat{\sigma}_{eg}^{j}\hat{\sigma}_{ge}^{i}\hat{\rho}_A - \hat{\rho}_A\hat{\sigma}_{eg}^{j}\hat{\sigma}_{ge}^{i}). \qquad \textbf{[S4]}$$

The Hamiltonian and the Lindblad are expressed in terms of the atomic coherence operator $\hat{\sigma}_{ge}^{j} = |g\rangle\langle e|$ between the ground and excited states of atom j. The Hamiltonian contains terms for the free-atom evolution, the coherent atom–atom interactions, and the classical drive, respectively; $\tilde{\Delta}_A = 2\pi\Delta_A = 2\pi(\nu_p - \nu_{\mathrm{D1}})$ is the detuning between the probe and the atomic angular frequencies, and Ω_j is the Rabi frequency for atom j caused by the GM field. The atom–atom spin exchange rate $J_{1\mathrm{D}}^{ji}$ is expressed in terms of the real part of the GM Green's function as

$$J_{1\mathrm{D}}^{ji} = \left(\frac{\mu_0\omega_p^2}{\hbar}\right)\mathbf{d}_j^{*}\cdot\mathrm{Re}\ \mathbf{G}(\mathbf{r}_j,\mathbf{r}_i,\omega_p)\cdot\mathbf{d}_i, \qquad \textbf{[S5]}$$

where $\omega_p = 2\pi\nu_p$, and $\mathbf{d}_j$ is the dipole matrix element of atom j. The Lindblad term is responsible for the dissipative interactions in the system, which include atomic decay into non-GMs (Γ') and GMs ($\Gamma_{1\mathrm{D}}^{ji}$). The decay rate into the GM is written in terms of the imaginary part of the Green's function as

$$\Gamma_{1\mathrm{D}}^{ji} = 2\left(\frac{\mu_0\omega_p^2}{\hbar}\right)\mathbf{d}_j^{*}\cdot\mathrm{Im}\ \mathbf{G}(\mathbf{r}_j,\mathbf{r}_i,\omega_p)\cdot\mathbf{d}_i. \qquad \textbf{[S6]}$$

For low atomic density along the PCW, the nonguided emission rate Γ' is not cooperative and is described here as a single-atom effect, with δ_{ji} as the Kronecker delta.

In the low saturation regime, the Heisenberg equations for the expectation value of the atomic coherences ($\langle\hat{\sigma}_{eg}\rangle = \sigma_{eg}$) can be solved for with the master equation leading to

$$\dot{\sigma}_{ge}^{j} = i\left(\tilde{\Delta}_A + \mathrm{i}\frac{\Gamma'}{2}\right)\sigma_{ge}^{j} + \mathrm{i}\ \Omega_j + \mathrm{i}\sum_{i=1}^{N}g_{ji}\ \sigma_{ge}^{i}, \qquad \textbf{[S7]}$$

where the complex coupling rate is

$$g_{ij} = J_{1\mathrm{D}}^{ij} + \frac{\mathrm{i}\Gamma_{1\mathrm{D}}^{ij}}{2} = \left(\frac{\mu_0\omega_p^2}{\hbar}\right)\mathbf{d}_i^{*}\cdot\mathbf{G}(\mathbf{r}_i,\mathbf{r}_j,\omega_p)\cdot\mathbf{d}_j, \qquad \textbf{[S8]}$$

which is the Green's function between atoms i and j projected onto the respective dipole matrix elements. In the steady-state solution, the time derivative is set to zero, and the result is the linear system of equations for the atomic coherences given in the text.

The electric field in the system can be expressed in terms of the input probe field $\mathbf{E}^{+}(\mathbf{r},\omega_p)$ and solutions for the atomic coherences (39):

$$\mathbf{E}^{+}(\mathbf{r},\omega_p) = \mathbf{E}_p^{+}(\mathbf{r},\omega_p) + \mu_0\omega_p^2\sum_{j=1}^{N}\mathbf{G}(\mathbf{r},\mathbf{r}_j,\omega_p)\cdot\mathbf{d}_j\sigma_{ge}^{j}. \qquad \textbf{[S9]}$$

An expression for the transmission through a quasi-1D structure can be derived by solving the steady-state system of equations in Eq. **S7** for the atomic coherences σ_{ge}^{j} and substituting them into Eq. **S9**. The expression can then be simplified in the case where the dipole moments are real, in which case $\mathfrak{g}$ is a complex symmetric matrix with eigenvectors and eigenvalues $\mathfrak{g}\ \mathbf{u}_\xi = \lambda_\xi\ \mathbf{u}_\xi$, and where the Green's function is well-represented by a 1D Green's function. The final result is (37)

$$\frac{t(\tilde{\Delta}_A,N)}{t_0(\tilde{\Delta}_A)}=\prod_{\xi=1}^{N}\left(\frac{\tilde{\Delta}_A+\mathrm{i}\Gamma'/2}{\tilde{\Delta}_A+\mathrm{i}\Gamma'/2+\lambda_\xi}\right), \quad \text{[S10]}$$

where $t_0(\tilde{\Delta}_A)$ is the transmission without atoms.

In the bandgap, the matrix $\mathfrak{g}$ of elements g_{ij} is well-approximated by

$$g_{ij}=\left(J_{1D}+\frac{\mathrm{i}\Gamma_{1D}}{2}\right)\cos\left(\frac{\pi x_i}{a}\right)\cos\left(\frac{\pi x_j}{a}\right)e^{-\kappa_x|x_i-x_j|}. \quad \text{[S11]}$$

As discussed in the text, when the interaction range $1/\kappa_x$ is much larger than the separation distance ($\kappa_x|x_i-x_j|\ll 1$), there is only a single atomic bright mode for which the frequency shift and GM decay rate are given by $\sum_{i=1}^{N}J_{1D}^{ii}$ and $\sum_{i=1}^{N}\Gamma_{1D}^{ii}$. The transmission spectrum for N atoms in the single bright mode approximation is given by

$$T(\Delta_A,N)=T_0(\Delta_A)\left|\frac{\tilde{\Delta}_A+\mathrm{i}\Gamma'/2}{\tilde{\Delta}_A+\mathrm{i}\Gamma'/2+\sum_i\left(J_{1D}^{ii}+\mathrm{i}\Gamma_{1D}^{ii}/2\right)}\right|^2, \quad \text{[S12]}$$

where $\tilde{\Delta}_A=2\pi\Delta_A=2\pi(\nu_p-\nu_{D1})$ is the detuning between the pump and the atomic frequency, and $T_0(\Delta_A)$ is the device transmission when no atoms are present.

Explicitly accounting for the atoms' positions by substituting Eq. **S11** into Eq. **S12**, we find that the transmission is given by

$$T(\Delta_A,N;x_1,\ldots,x_N)/T_0(\Delta_A)=\left|\frac{\Delta_A'+\mathrm{i}\Gamma'/2}{\Delta_A'+\mathrm{i}\Gamma'/2+\sum_{j=1}^{N}\left(J_{1D}+\mathrm{i}\Gamma_{1D}/2\right)\cos^2\left(\frac{x_j\pi}{a}\right)}\right|^2. \quad \text{[S13]}$$

We have defined $\Delta_A'\equiv\tilde{\Delta}_A+\Delta_0$ to account for the AC Stark shift Δ_0 of the atoms because of the dipole trap.

To accurately model the experimental conditions, we average the transmission model over atom positions and atom number. During a single measurement, the atoms are free to move along the length of the device over the range $2\Delta x_A$ as in Fig. S5*A*, evenly sampling the Bloch function. We let $\langle T(\Delta_A,N;x_1,\ldots,x_N)\rangle_x$ be an average over all positions, that is,

$$\langle T(\Delta_A,N;x_1,\ldots,x_N)\rangle_x=T_0(\Delta_A)\int_0^a \mathrm{d}x_1\ldots\mathrm{d}x_N\left|\frac{\Delta_A'+\mathrm{i}\Gamma'/2}{\Delta_A'+\mathrm{i}\Gamma'/2+\sum_{j=1}^{N}\left(J_{1D}+\mathrm{i}\Gamma_{1D}/2\right)\cos^2\left(\frac{x_j\pi}{a}\right)}\right|^2.$$

We repeat the measurement multiple times for each frequency Δ_A. Each experiment can have a different number of atoms, and therefore, we average the transmission expression over a Poisson distribution $P_{\bar{N}}(N)$, which is a function of the average atom number $\bar{N}$. The transmission model averaged over both atom positions and atom numbers is given by

$$\langle T(\Delta_A,N;x_1,\ldots,x_N)\rangle_{x,N}=T_0(\Delta_A)\sum_N P_{\bar{N}}(N)\langle T(\Delta_A,N;x_1,\ldots,x_N)\rangle_x. \quad \text{[S14]}$$

This expression is the final form of the transmission model that we use to fit the atomic spectra.

Assuming $\bar{N}=3.0$, which is obtained from the atom decay rate measurement, we fit the TE atomic spectra with Eq. **S14** and extract Γ_{1D}, J_{1D}, Γ', and Δ_0 for each frequency. We show the values of Γ_{1D} and J_{1D} in Fig. 4*A*. We show the AC Stark shift and nonguided decay rate in Fig. S6.

The average of the nonguided decay rate Γ' for the TE data outside the bandgap is $\Gamma'=2\pi\times 9.1$ MHz, which is significantly larger than the expected value from the FDTD simulation, $\Gamma'=2\pi\times 5.0$ MHz. This additional inhomogeneous broadening could be caused by finite temperature of the trapped atoms, vector shifts from circular light in the SI beam, atom density-dependent collisional broadening, stray magnetic fields, and electric fields from charges in the dielectric. We estimate the contributions individually and find that they likely do not explain the extraneous broadening. We note that the estimate of temperature of trapped atoms could be improved in the future (49), and it may help shed light on our excess broadening.

Interestingly, the fitted Γ' increases in the bandgap and is as high as $\Gamma'=2\pi\times 16$ MHz for the last measured point. One possible explanation is that this is because of the breakdown of the single bright mode approximation, because coupling to multiple collective atomic modes should result in a broadened linewidth. Another possibility is that, because there is a large extinction of the TE mode in the bandgap, there might be some mixing between the TE and TM modes.

We also measure transmission spectra for the TM mode, which have band edges that are far-detuned from the Cs transitions. The transmission in this waveguide regime is described by an optical depth (OD) model

$$\frac{T}{T_0}=\exp\left[\frac{-\mathrm{OD}}{1+\left(\frac{2\Delta_A'}{\Gamma_{1D}^{TM}+\Gamma'}\right)^2}\right], \quad \text{[S15]}$$

where the resonant OD is given by $\mathrm{OD}=2\bar{N}\Gamma_{1D}^{TM}/\tilde{\Gamma}'$. We fit the TM spectra with this model and extract Γ', Δ_0, and Γ_{1D}^{TM} (assuming $\bar{N}=3$). The values of Γ' and Δ_0 are shown with the TE data in Fig. S6. The averaged Γ_{1D}^{TM} value is 0.044 Γ_0, which is $\sim$30 times smaller than Γ_{1D} for the TE mode at the first resonance ν_1 and clearly shows the enhanced interaction because of the PCW.

5. Simple Transmission Model. In the text, we fit atomic transmission spectra with the averaged transmission model from Eq. **S14** to extract the peak GM decay rate Γ_{1D} and frequency shift J_{1D}. In this section, we fit the spectra with a transmission model that involves no averaging, and we extract an effective decay rate Γ_{1D}^{eff} and frequency shift J_{1D}^{eff}, which will be smaller than the corresponding peak values because of the averaging of the $\cos^2(\pi x/a)$ Bloch function as the atoms move along the x axis of the trap. In the single bright mode approximation discussed in the text, the transmission for a single collective mode with total decay rate A and frequency shift B is given by

$$\frac{T(\Delta_A)}{T_0(\Delta_A)}=\left|\frac{\Delta_A'+\mathrm{i}\Gamma'/2}{\Delta_A'+B+\mathrm{i}\,(\Gamma'+A)/2}\right|^2. \quad \text{[S16]}$$

Here, the detuning Δ_A' includes the AC stark shift $\Delta_A'=\Delta_A+\Delta_0$. Because the average number of atoms $\bar{N}\approx 3$ is measured independently in a decay rate measurement, the collective rates A and B are related to the effective rates by $A=\bar{N}\Gamma_{1D}^{eff}$ and $B=\bar{N}J_{1D}^{eff}$. Examples of the fitted spectra for atoms outside and inside the band gap are shown in Fig. S7. The translucent lines in Fig. S7 are the expected signals for average atom numbers of $\bar{N}=1$ and $\bar{N}=9$.

The fitted values of A and B are plotted for each detuning from the band edge Δ_{BE} in Fig. S8*A*. The results are qualitatively similar to the corresponding plot in Fig. 4*A*, except that the effective rates $A=\bar{N}\Gamma_{1D}^{eff}$ and $B=\bar{N}\Gamma_{1D}^{eff}$ are scaled down by $\eta=0.42$ because of the modulation of the Bloch function $\cos^2(\pi x/a)$. The solid lines in Fig. S8*A* are the same theoretical curves as in Fig. 4*A*, except that they are scaled by $\eta=0.42$.

The ratio of $A/B=\Gamma_{1D}^{eff}/J_{1D}^{eff}$ is plotted in Fig. S8*B*. Because the scale factors η cancel, the result is in good agreement with the corresponding plot of $\mathcal{R}=\Gamma_{1D}/J_{1D}$ in Fig. 4*B*. The black theory curve in Fig. S8*B* is the same as in Fig. 4*B*. Whereas the peak decay rate and frequency shift are sensitive to the specific model, the ratio of dissipative to coherent coupling is mostly model insensitive.

6. Atom Decay Measurement. We exploit the superradiance of atoms trapped near the alligator PCW to determine the mean atom number $\bar{N}$ and the peak atom decay rate Γ_{1D} (at ν_1) into the GMs.

As established in ref. 21, the total exponential decay rate of the atoms is $\bar{\Gamma}_{tot}(\bar{N})=\bar{\Gamma}_{SR}(\bar{N})+\bar{\Gamma}_{tot}^{(1)}$, where $\bar{\Gamma}_{SR}$ is the $\bar{N}$-dependent superradiance decay rate, and $\bar{\Gamma}_{tot}^{(1)}$ is the observed single-atom decay rate. We note that, when $\bar{N}\ll 1$, $\bar{\Gamma}_{tot}\sim\bar{\Gamma}_{tot}^{(1)}=\bar{\Gamma}_{1D}+\Gamma'$, because only the single-atom decay rates $\bar{\Gamma}_{1D}$ into the GM and Γ' into the environment remain; Γ' is numerically calculated to be $2\pi\times 5.0$ MHz for the Cs D_1 line at the trapping site near the PCW (21).

We excite the atoms with a weak resonant light pulse through the GM, whereas the first resonance ν_1 near the band edge is aligned with the Cs D_1 line. Pulse properties are as in ref. 21. The subsequent fluorescence decay rates $\bar{\Gamma}_{tot}$ are determined through exponential fits. By varying the trap holding time t_m after loading, the mean atom numbers for the decay measurements are varied. The decay rates are empirically fitted in an exponential form as a function of holding time t_m (21) : $\bar{\Gamma}_{tot}(t_m)=\bar{\Gamma}_{SR}e^{-t_m/\tau_{SR}}+\bar{\Gamma}_{tot}^{(1)}$, as shown in Fig. S9. From the fitted asymptotic value of the decay rates, we deduce that the apparent single-atom decay rate is $\bar{\Gamma}_{1D}=(1.12\pm 0.14)\Gamma'$.

Because the atoms are randomly distributed along the x direction in the trap, the observed decay curves are results after spatially averaging the coupling rates $\Gamma_{1D}(x)$. Assuming a uniform distribution of N atoms around the center of the PCW, a more detailed model specifies the form of fluorescence intensity decay as (21)

$$\mathcal{I}_N(t)=\gamma^2 e^{-(N\gamma+\Gamma')t}\cdot I_0(\gamma t)^{N-2}\cdot\left[\frac{N(N+1)}{4}I_0(\gamma t)^2-\left(\frac{N}{4\gamma t}+\frac{N^2}{2}\right)I_0(\gamma t)I_1(\gamma t)+\frac{N(N-1)}{4}I_1(\gamma t)^2\right], \quad \text{[S17]}$$

where $\gamma=\Gamma_{1D}/2$, and I_k is the modified Bessel function. Numerically simulating the decay of single atoms in the trap by using $\mathcal{I}_1(t)$, we compare between the exponentially fitted value $\bar{\Gamma}_{1D}$ and the value of Γ_{1D} used for $\mathcal{I}_1(t)$, which yields a ratio of $\bar{\Gamma}_{1D}/\Gamma_{1D}=0.81$. This ratio is consistent with the ratio of 0.8 ± 0.3 from measurement at long hold time $t_m=94$ ms, when single-atom decay predominates (shown as the asymptote in Fig. S9). Based on the values of $\bar{\Gamma}_{1D}$ deduced above, we conclude that $\Gamma_{1D}=(1.4\pm 0.2)\Gamma'$.

At early holding times, the atom number N noticeably fluctuates around some mean values $\bar{N}\gtrsim 1$. To capture this $\bar{N}$-dependent variation, we fit the decay curves by averaging $\mathcal{I}_N(t)$ with weight function of Poisson distribution probability $P_{\bar{N}}(N)$ (21). The fitting parameter here is $\bar{N}$, whereas we fix the value of Γ_{1D} in Eq. **S17**. The fit is consistent with $\bar{N}=3.0\pm 0.5$ at $t_m=4$ ms when we carry out the transmission spectra measurement. Based on the trap lifetime $\tau=30$ ms, we further deduce that $\bar{N}\sim 0.1$ at $t_m=94$ ms.

The linear $\bar{N}$ dependence of superradiance is given by $\bar{\Gamma}_{SR}=\eta\cdot\bar{N}\cdot\Gamma_{1D}$, where $\eta=0.36\pm 0.06$ is some linear coefficient that has a value is consistent with that reported in ref. 21.

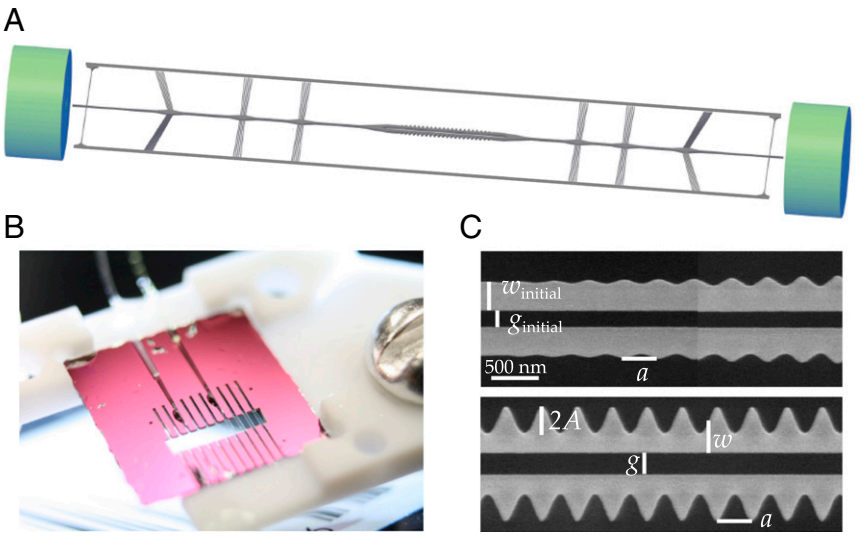

Fig. S1. Alligator PCW chip and device overview. (*A*) Schematic of the entire device. The alligator PCW is at the center. Optical fibers (green) on both ends couple light into and out of the waveguide. The waveguide is surrounded by supporting and cooling structures. (*B*) Image of a 10×10-mm PCW chip. Multiple waveguides stretch across the window of the chip, with the PCWs at the center of the window. The window provides optical access for trapping and cooling atoms around the device. Reproduced from ref. 33, with the permission of AIP Publishing. (*C*) Overview of device variables. The lattice constant for the entire device is $a=370$ nm. The device dimensions are measured with an SEM and calibrated to the lattice constant. The device dimensions are $w=310\pm 10$ nm, $2A=262\pm 10$ nm, $g=220\pm 10$ nm, $w_{initial}=268\pm 15$ nm, and $g_{initial}=165\pm 10$ nm. The thickness of the SiN is 185 ± 5 nm. The index of refraction for Si_3N_4 is $n=2.0$ around our frequencies of interest.

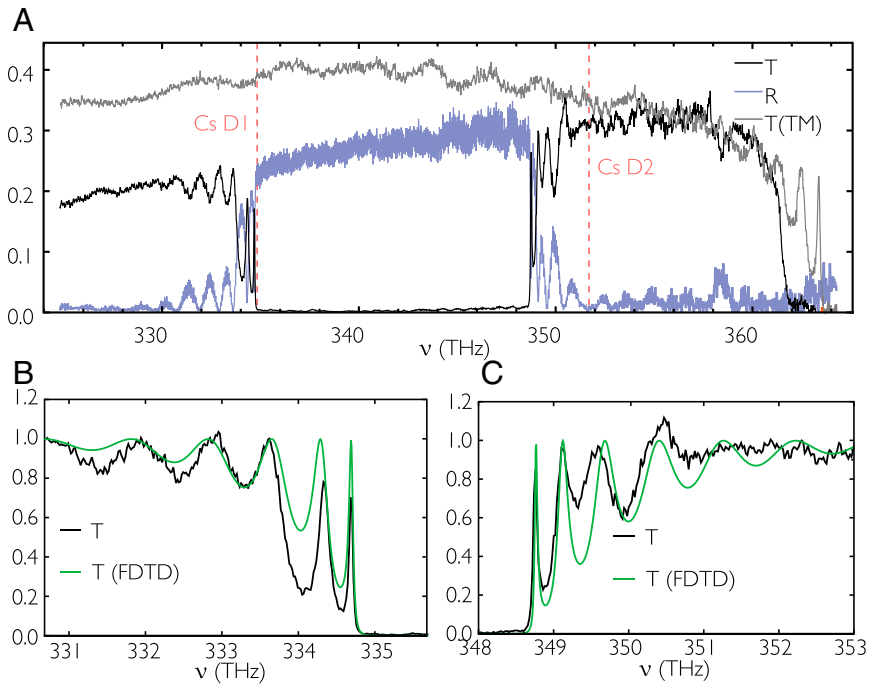

Fig. S2. Measured and simulated transmission and reflection spectra. (*A*) Transmission (black) and reflection (blue) spectra through the entire chip for the TE mode (polarization in the plane of the device). The red dashed lines are the Cs D_1 (335.1 THz) and D_2 (351.7 THz) lines. The TE transmission efficiency through the entire device near the dielectric band edge is ~23%, indicating that the single-pass efficiency from the fiber to device is approximately 49%. Most of the loss is caused by the waveguide to fiber coupling section. The gray line is the TM transmission (polarization perpendicular to the plane of the device). Note that the lower band edge of the TM mode is visible at around 365 THz but far detuned from both Cs $D_{1,2}$ transitions. (*B* and *C*) TE transmission data are normalized and compared with an FDTD simulation (37). The simulation uses the measured device parameters in Fig. S1 that are adjusted within the uncertainty of the measurements so that the positions of the first resonances match those in the measured spectra.

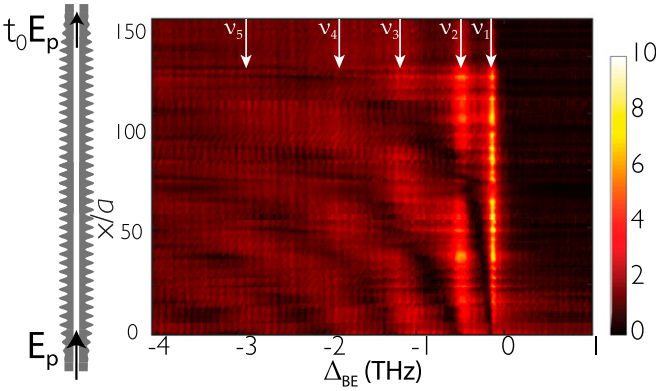

Fig. S3. Normalized magnitude of the scattered electric field of the PCW for frequencies $\Delta_{BE} = \nu_p - \nu_{BE}$ around the band edge. The schematic in *Left* shows the PCW with the number of unit cells reduced by five.

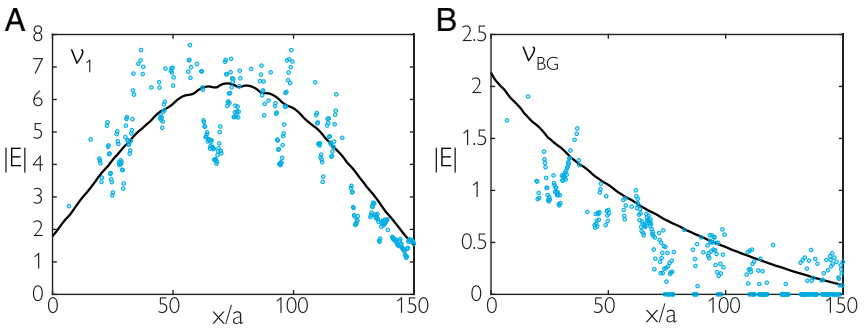

Fig. S4. The electric field magnitude in (*A*) the PCW at the first resonance ν_1 and (*B*) the bandgap $\nu_{BG} = \nu_{BE} + 60$ GHz. The points show measured data, and the black lines are from an FDTD simulation. The electric field magnitude $|E|$ is normalized by the electric field magnitude far from the band edge; thus, these plots give the enhancement of $|E|$ relative to the waveguide regime.

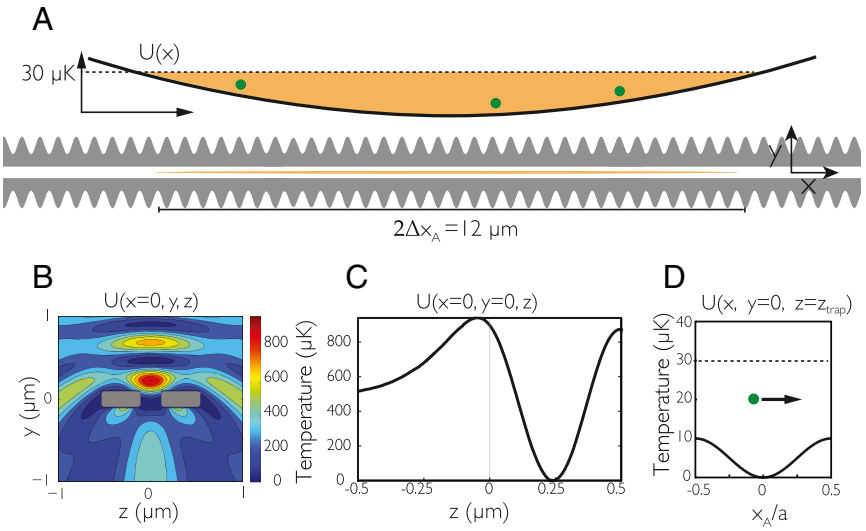

Fig. S5. (*A*) Schematic of the atoms in the SI trap. Given the estimated atom temperature of 30 μK, we infer that the atoms are confined to a length of $2\Delta x_A = 12$ μm along the *x* axis. (*B–D*) Far-off–resonance optical trap (FORT) potentials for the SI trap simulation (*B*) in the *y–z* plane (21), (*C*) along the *z* axis, and (*D*) along the *x* axis.

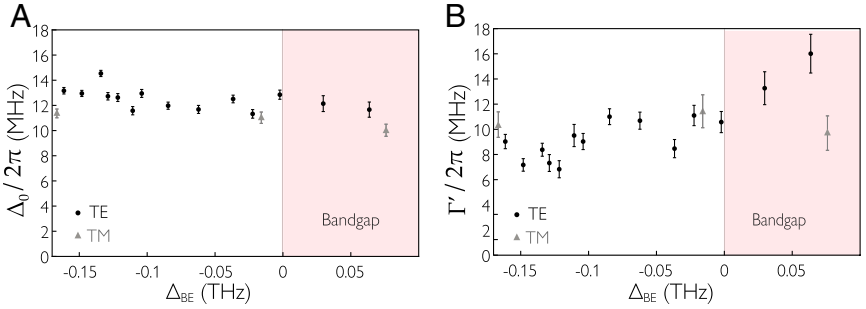

Fig. S6. Fitted values from the averaged transmission model for TE (black circles) and TM (gray triangles) spectra. (*A*) Fitted AC Stark shift Δ_0. (*B*) Fitted Γ'.

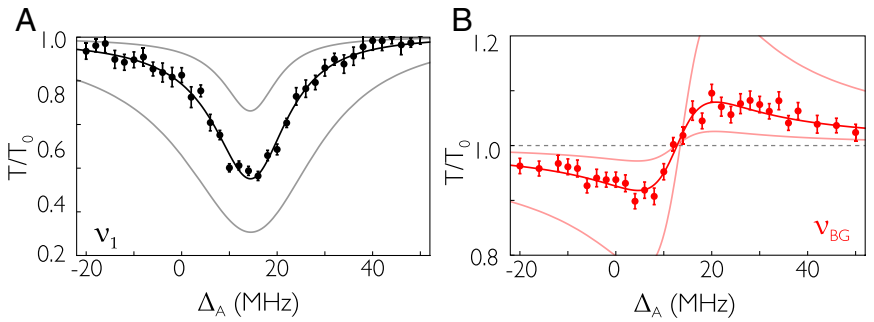

Fig. S7. Fits of transmission spectra with the model in Eq. **S16** for when the atomic resonance frequency is aligned to (*A*) the first resonance and (*B*) in the bandgap. From the decay rate measurement, the average number of atoms is $\bar{N} \approx 3$ for the full (central) curves in *A* and *B*, while the translucent curves give the expected spectra for $\bar{N} = 1$ and $\bar{N} = 9$ atoms.

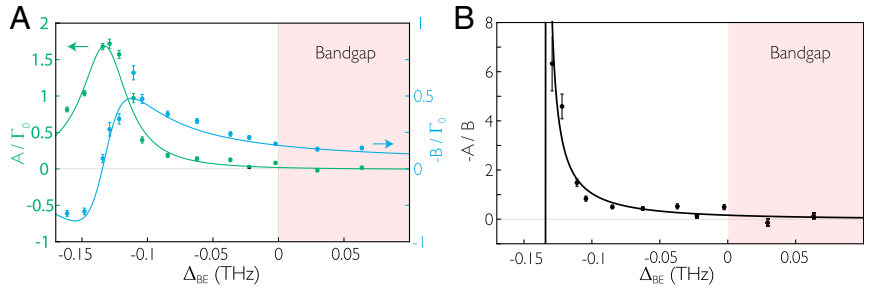

Fig. S8. (*A*) Fitted values for the effective collective decay rates *A* and frequency shifts *B* for various detunings from the band edge Δ_{BE}. The solid lines are the expected results for the peak values as in Fig. 4*A*, except scaled down by $\eta = 0.42$. (*B*) Ratio $A/B = \Gamma_{1D}^{eff}/J_{1D}^{eff}$ along with the theoretical prediction for the peak ratio Γ_{1D}/J_{1D} from Fig. 4*B*.

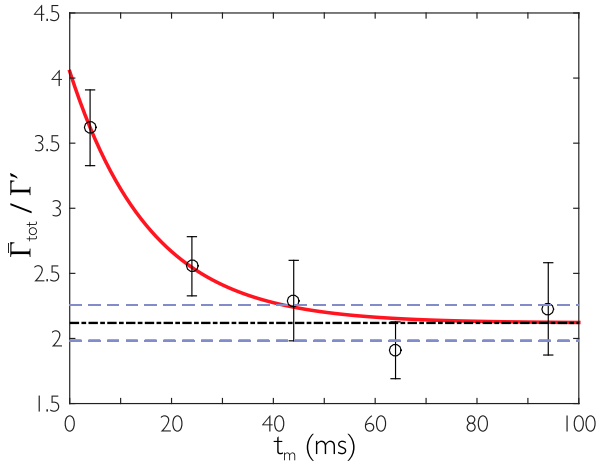

Fig. S9. Total decay rates as a function of holding time t_m. The red solid curve is the empirical fit, and the dash-dot line represents the fitted asymptotic total decay rate at very long times. The blue dashed lines specify fitted error boundaries. The fit yields $\tau_{SR} = 16$ ms, $\bar{\Gamma}_{SR} = 1.5\Gamma'$, and the asymptote $\bar{\Gamma}_{tot}^{(1)}/\Gamma' = 2.12 \pm 0.14$.